Electronic Supplementary Information

Morphology and facet effects on the charge and discharge mechanisms in $FeSe_2$-based lithium-ion storage

Chih-Hsueh Li, Yu-Bo Hung, Bo-Hao Chen, Vandana Meena, Wei-Cheng Chu, Hsing-Yu Tuan and Michael H. Huang**

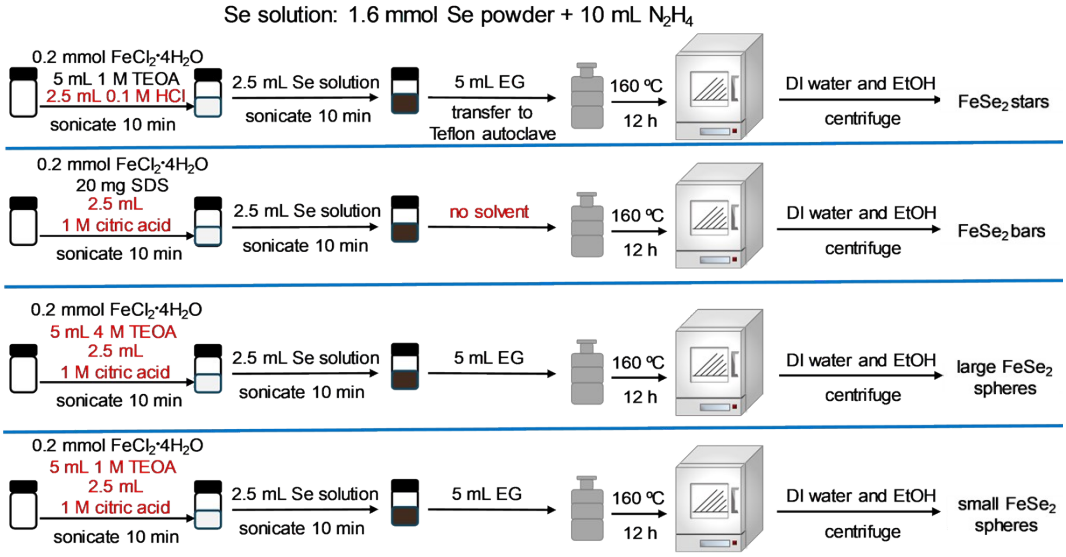

Fig. S1 Reaction conditions for the synthesis of different $FeSe_2$ crystals.

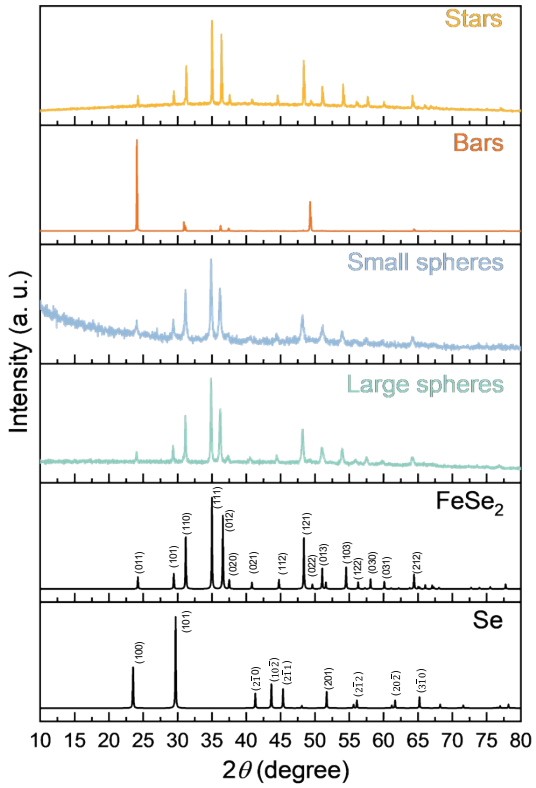

Fig. S2 In-house XRD patterns of $FeSe_2$ crystals.

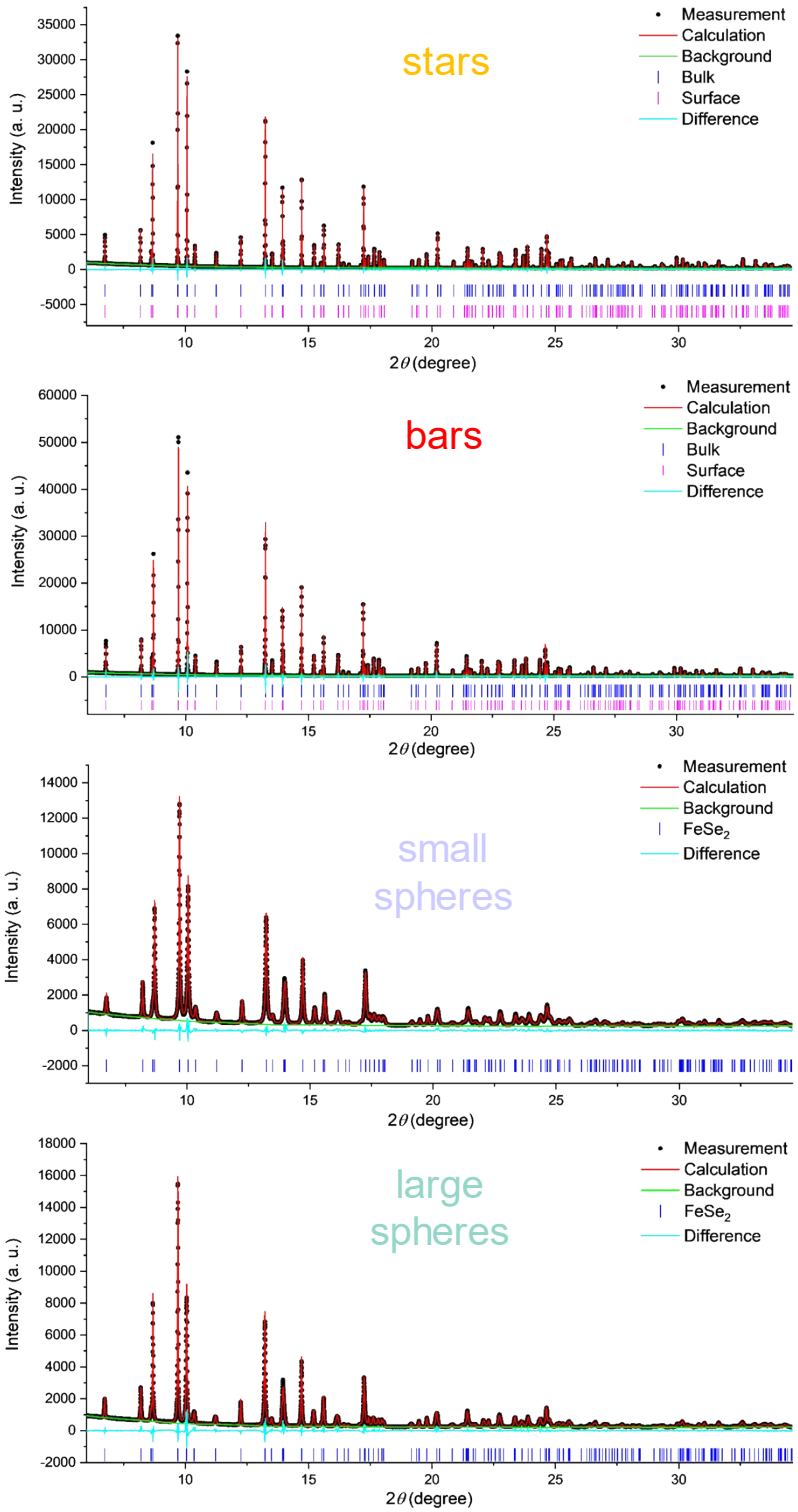

Fig. S3 Rietveld refinement results of different $FeSe_2$ crystals.

Table S1 Crystallographic data of as-synthesized $FeSe_2$ crystals

Sample	Small spheres	Large spheres	Bars		Stars	
	one phase		bulk	surface	bulk	surface
Wavelength (Å)	0.43503					
Crystal system	orthorhombic					
Space group	Pmnn					
a (Å)	3.57248(5)	3.57588(6)	3.584005(12)	3.58463(4)	3.584294(6)	3.584289(24)
b (Å)	4.82219(8)	4.81735(8)	4.800940(15)	4.80715(7)	4.800297(1)	4.80439(5)
c (Å)	5.79466(7)	5.79194(7)	5.782552(15)	5.78554(5)	5.782256(1)	5.78370(4)
2θ range (°)	6–34.6		6–34.76		6–34.6	
Volume ($Å^3$)	99.826(4)	99.774(3)	99.4980(6)	99.6954(22)	99.4876(3)	99.5972(16)
d-spacing resolution (Å)	0.732	0.732	0.730		0.734	
Wt (%)	100		71.61	28.39	68.84	31.16
Mean μ strain	10970.0	8121.4	1376.5	2424.8	1199.9	1973.9
Zero point shift (°)	0.0003	0.0014	0.0007		0.0004	
R (F^2) (%)	4.114	4.581	6.935	7.678	2.845	5.314
wRp (%)	4.648	6.811	7.571		4.428	

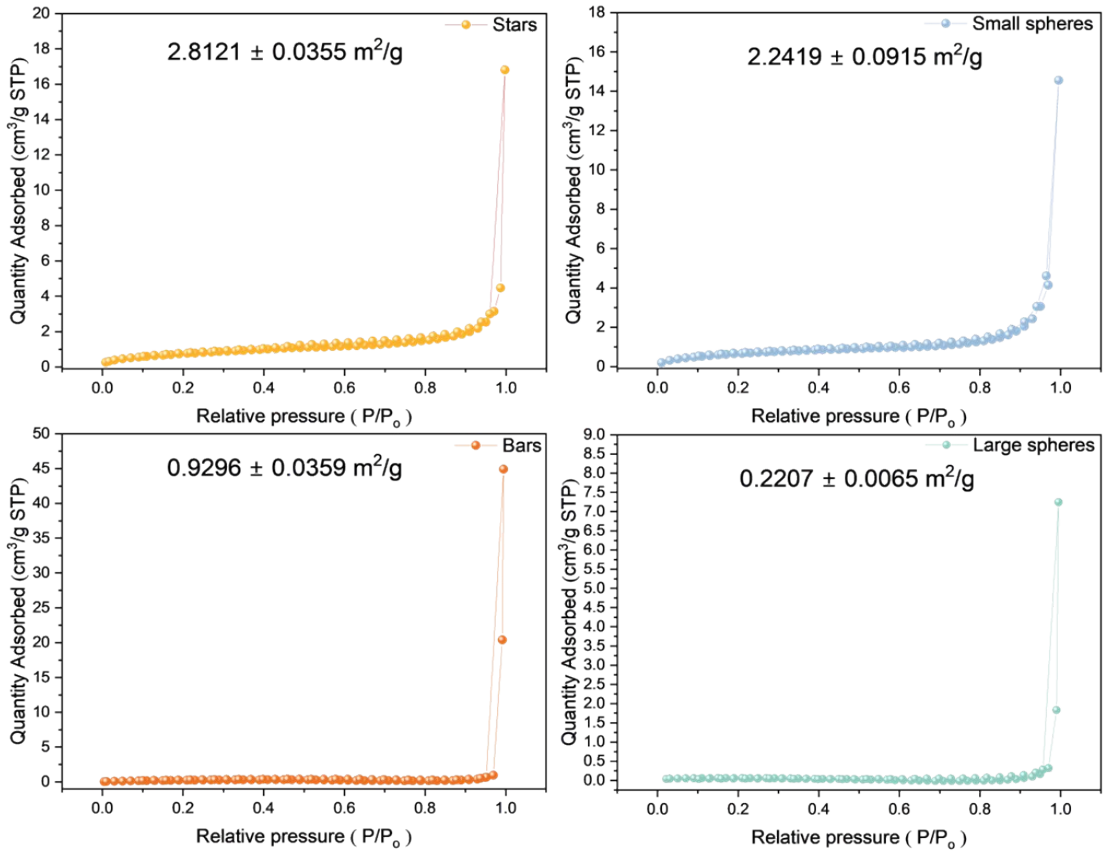

Fig. S4 Nitrogen adsorption−desorption isotherms of different $FeSe_2$ crystals.

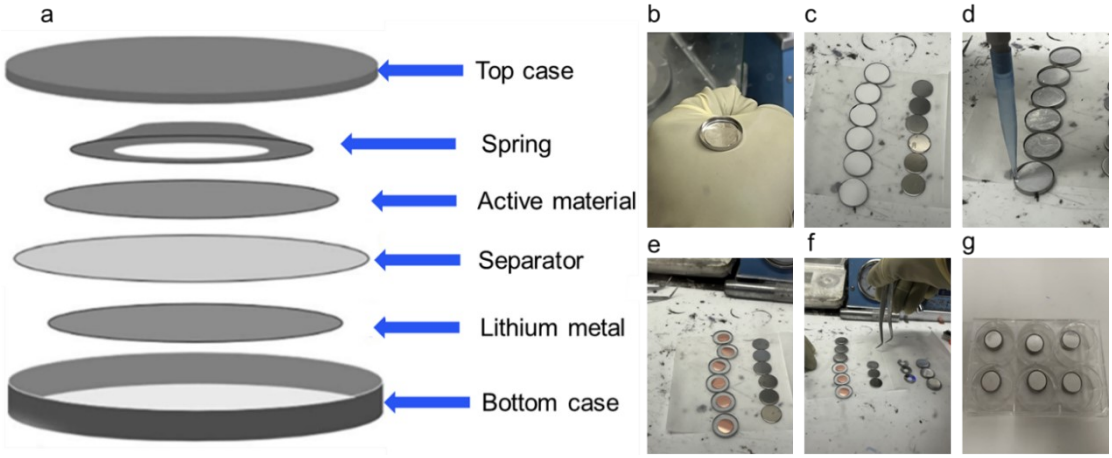

Fig. S5 (a) Schematic illustration of the components used in lithium ion battery assembly. (b) Placing lithium into the bottom case. (c) Adding a separator over the lithium metal. (d) Adding the electrolyte. (e) Placing a copper foil coated with the active material, ensuring that the active material side faces downward. (f) Placing a spring and the top cover in sequence to complete the coin cell assembly. (g) The assembled lithium ion battery.

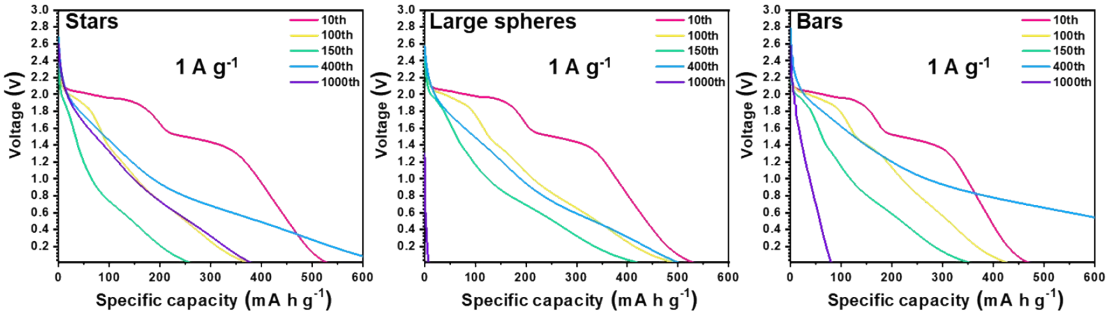

Fig. S6 Galvanostatic discharge curves of stars, large spheres, and bars for the 10th, 100th, 150th, 400th, and 1000th cycles at a current density of 1 A g^{-1}.

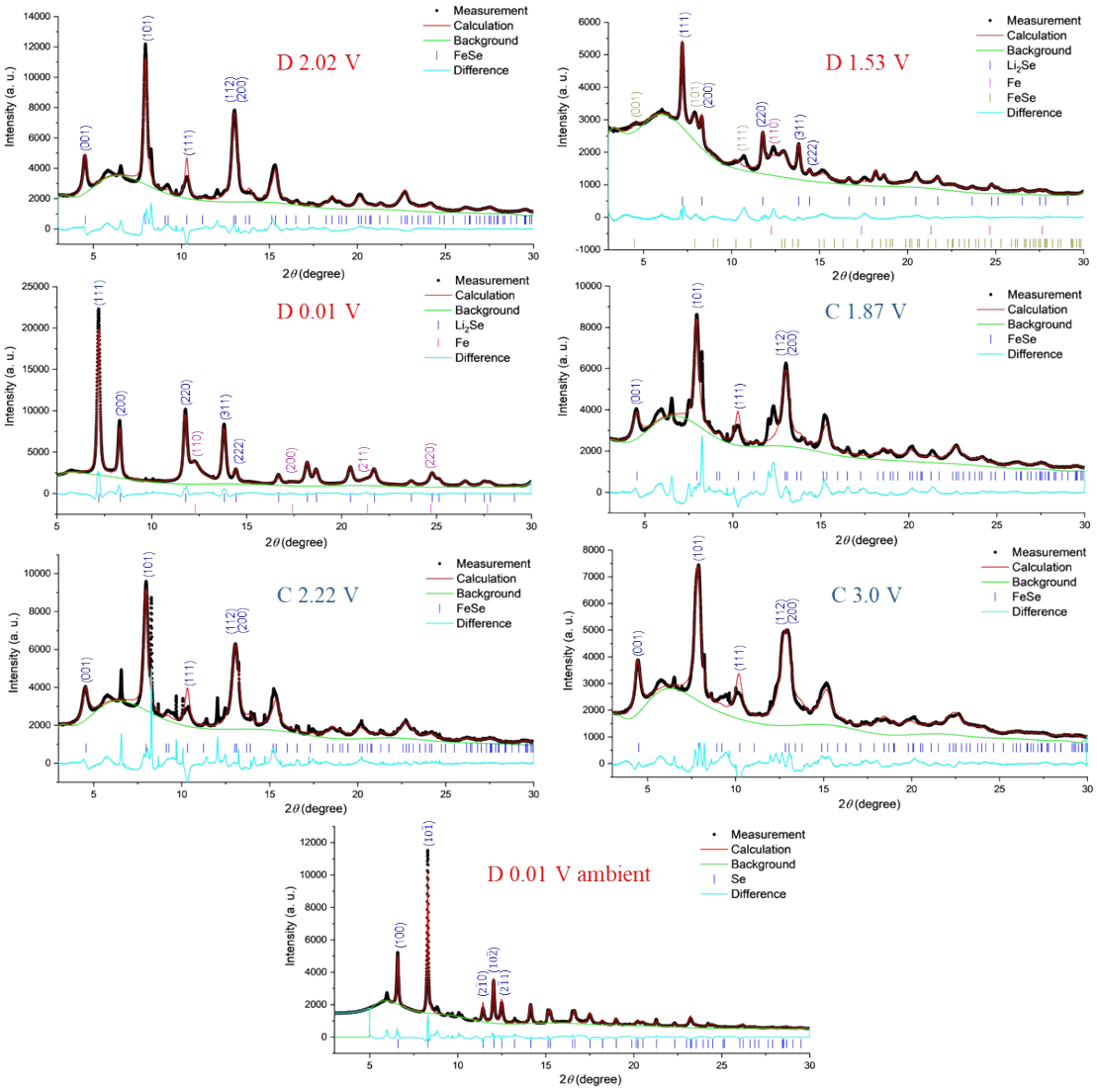

Fig. S7 Rietveld refinement results of FeSe, Li_2Se, Fe, and Se at different potentials in the 3rd cycle of stage I.

Table S2 Crystallographic data of FeSe at different potentials in the 3rd cycle (stage I) (C = charging)

Entry	C 3 V	C 2.22 V	C 1.87 V	D 2.02 V
Compound	FeSe			
Wavelength (Å)	0.43503			
Crystal system	tetragonal			
Space group	P4/nmm			
a (Å)	3.8362(8)	3.8095(15)	3.8156(14)	3.8159(5)
c (Å)	5.662(20)	5.476(5)	5.491(4)	5.4971(14)
2θ range (°)	3–30			
Volume ($Å^3$)	81.913(20)	79.47(10)	79.939(28)	80.043(14)
d-spacing resolution (Å)	0.840	0.842	0.843	0.843
Equatorial μ strain	72794.1	47553.7	54970.7	34723.5
Axial μ strain	167049.1	153208.2	179972.0	102454.6
μ strain unique axis (hkl)	001			
Size (μm)	0.0424	0.0249	0.053	0.0541
Zero point shift (°)	0.002	0.0068	0.002	0.002
$R(F^2)$ (%)	4.285	7.294	9.729	6.599
wRp (%)	6.270	8.741	8.284	7.024

Table S3 Crystallographic data of the materials at D 1.53 V in the 3rd cycle (stage I)

Entry	D 1.53V		
Compound	Li_2Se	Fe	FeSe
Wavelength (Å)	0.43503		
Crystal system	Cubic	Cubic	Tetragonal
Space group	Fm-3m	Im-3m	P4/nmm
a (Å)	5.9979(4)	2.8790(29)	3.8335(27)
c (Å)	X	X	5.563(9)
2θ range (°)	3–30		
Volume ($Å^3$)	215.78(4)	23.86(7)	81.76(6)
d-spacing resolution (Å)	0.845		
Wt (%)	0.316	0.225	0.459
Equatorial μ strain	15105.3	3724.4	64612.7
Axial μ strain	22359.2	7987.0	197660.2
μ strain unique axis (hkl)	200	200	001
$R(F^2)$ (%)	6.591	4.609	2.928
wRp (%)	3.154		
Size (μm)	0.0299	0.0028	0.0118
Zero point shift (°)	0.001		
Z	4	2	2
MW (g/mol)	92.84	55.85	134.84
S	0.1863	0.4411	0.3726

Table S4 Crystallographic data of the materials at D 0.01 V and D 0.01 V ambient in the 3rd cycle (stage I) (D = discharging)

Entry	D 0.01 V		D 0.01 V ambient
Compound	Li_2Se	Fe	Se
Wavelength (Å)	0.43503		
Crystal system	Cubic	Cubic	Hexagonal
Space group	Fm-3m	Im-3m	P3121
a (Å)	6.00205(21)	2.8752(8)	4.3677(8)
			4.9594(3)
c (Å)	X	X	
2θ range (°)	5–30		5–30
Volume ($Å^3$)	216.221(22)	23.770(19)	81.936(21)
d-spacing resolution (Å)	0.866		0.855
Wt (%)	0.649	0.351	100
Equatorial μ strain	14494.1	1000	15234.7
Axial μ strain	18699.5	1000	28614.5
μ strain unique axis (hkl)	200	200	200
Zero point shift (°)	0.008		0.0092
$R(F^2)$ (%)	1.355	1.871	10.711
wRp (%)	4.409		5.783
Z	4	2	3
MW (g/mol)	92.84	55.85	78.96
S	0.3575	0.6425	X

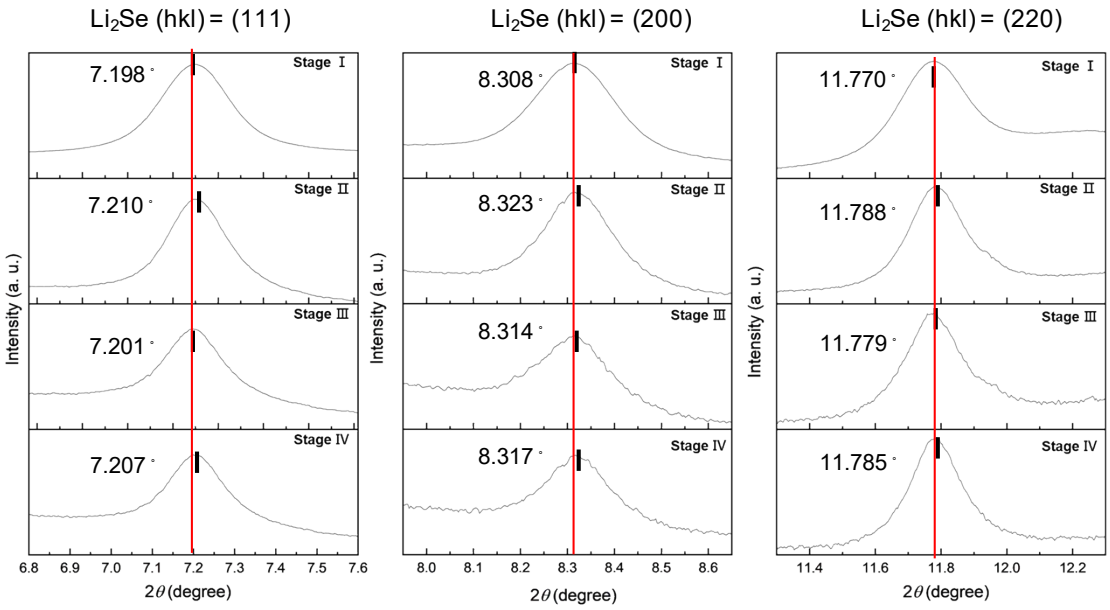

Fig. S8 Ex-situ high-resolution (111), (200) and (220) diffraction peaks of Li_2Se in the four stages at 0.01 V.

Table S5 Crystallographic data of the materials at D 0.01 V in the 150th cycle (stage II)

Entry	D 0.01 V	
Compound	Li_2Se	Fe
Wavelength (Å)	0.43503	
Crystal system	Cubic	Cubic
Space group	Fm-3m	Im-3m
a (Å)	5.99288(16)	2.8803(16)
c (Å)	X	X
2θ range (°)	5–29	
Volume (Å^3)	215.232(17)	23.90(4)
d-spacing resolution (Å)	0.903	
Wt (%)	66.5	33.5
Equatorial μ strain	15351.9	291365.8
Axial μ strain	20171.8	129649.9
μ strain unique axis (hkl)	200	200
Zero point shift (°)	0.0021	
R(F^2) (%)	4.833	3.914
wRp (%)	1.918	
Z	4	2
MW (g/mol)	92.84	55.85
S	0.3734	0.6266

Table S6 Crystallographic data of the materials at C 3.0 V in the 150th cycle (stage II)

Entry	C 3.0 V	
Compound	Fe	FeSe
Wavelength (Å)	0.43503	
Crystal system	Cubic	Tetragonal
Space group	Fm-3m	P4/nmm
a (Å)	3.61567(15)	3.790(4)
c (Å)	X	5.860(7)
2θ range (°)	3–30	
Volume (Å^3)	47.268(6)	84.18(17)
d-spacing resolution (Å)	0.846	
Wt (%)	12.7	87.3
Equatorial μ strain	11035.1	363188.5
Axial μ strain	3449.1	329295.6
μ strain unique axis (hkl)	001	001
Zero point shift (°)	0.001	
R(F^2) (%)	5.580	0.660
wRp (%)	2.183	
Size (μm)	0.0391	0.05
Z	4	2
MW (g/mol)	55.85	134.81
S	0.1498	0.8502

Table S7 Crystallographic data of the materials at D 0.01 V in the 400th cycle (stage III)

Entry	D 0.01V	
Compound	Li_2Se	Fe
Wavelength (Å)	0.43503	
Crystal system	Cubic	Cubic
Space group	Fm-3m	Im-3m
a (Å)	6.0000(7)	2.885(4)
c (Å)	X	X
2θ range (°)	5–29	
Volume (Å^3)	216.00(8)	24.01(9)
d-spacing resolution (Å)	0.905	
Wt (%)	0.296	0.704
Equatorial μ strain	20055.6	216064.4
Axial μ strain	28430.6	178422.8
μ strain unique axis (hkl)	200	200
Zero point shift (°)	0.00015	
R(F^2) (%)	11.753	4.359
wRp (%)	3.622	
Z	4	2
MW (g/mol)	92.84	55.85
S	0.1124	0.8876

Table S8 Crystallographic data of the materials at D 0.01 V in the 1000th cycle (stage IV)

Entry	D 0.01V	
Compound	Li_2Se	Fe
Wavelength (Å)	0.43503	
Crystal system	Cubic	Cubic
Space group	Fm-3m	Im-3m
a (Å)	5.9942(6)	2.889(4)
c (Å)	X	X
2θ range (°)	6–30	
Volume (Å^3)	215.38(7)	24.11(10)
d-spacing resolution (Å)	0.865	
Wt (%)	0.364	0.636
Equatorial μ strain	15248.3	188816.7
Axial μ strain	24816.4	182492.3
μ strain unique axis (hkl)	200	200
Zero point shift (°)	0.00015	
R(F^2) (%)	12.262	5.634
wRp (%)	3.397	
Z	4	2
MW (g/mol)	92.84	55.85
S	0.1467	0.8533

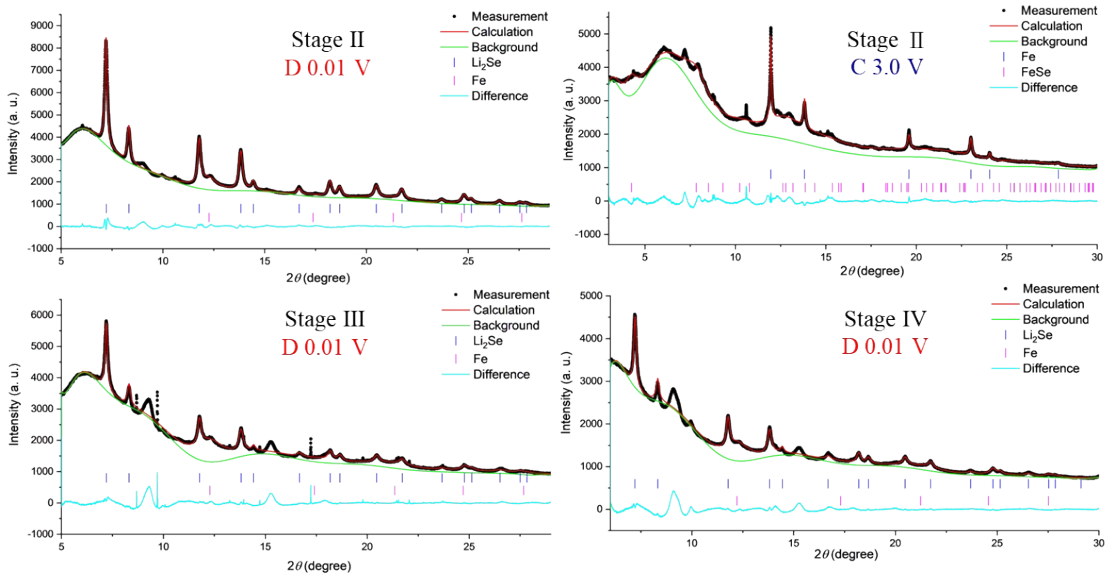

Fig. S9 Rietveld refinement results of Li_2Se, Fe, and FeSe at different potentials in the 150th cycle (stage II), 400th cycle (stage III), and 1000th cycle (stage IV).

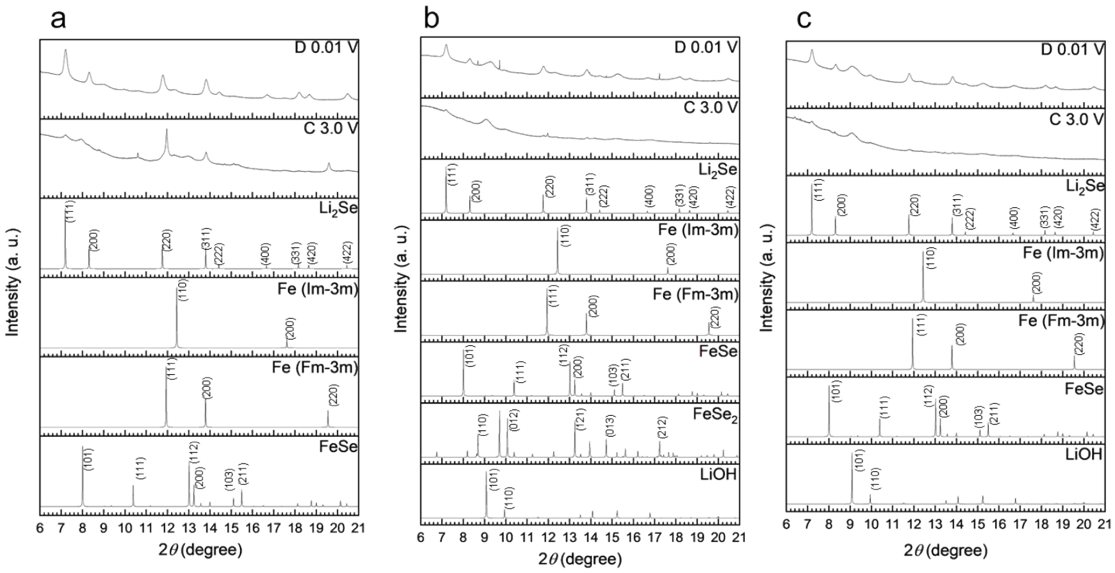

Fig. S10 Synchrotron XRD patterns at different potentials in the (a) 150th cycle (stage II), (b) 400th cycle (stage III), and (c) 1000th cycle (stage IV).

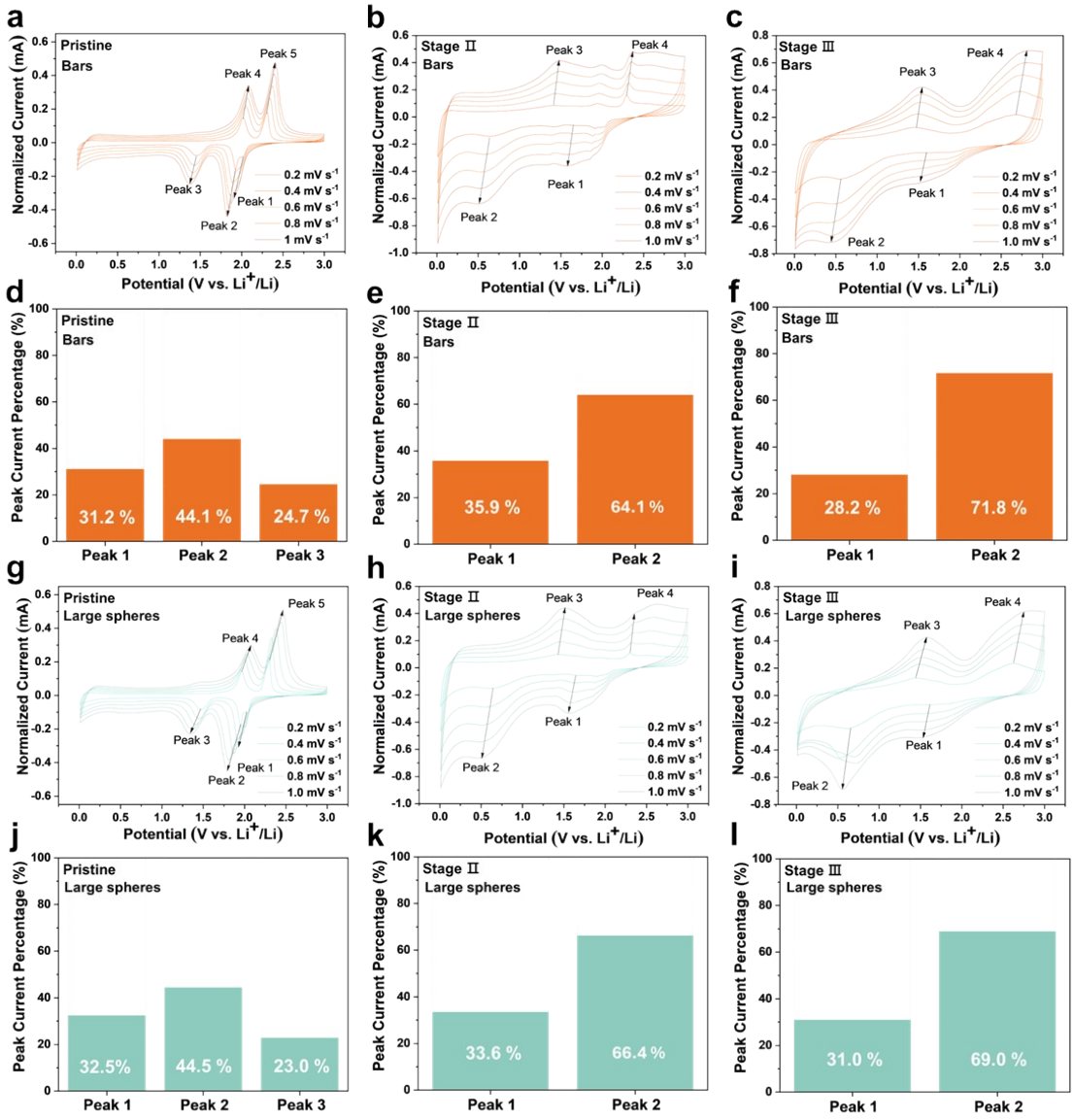

Fig. S11 Reduction peak current analysis. (a–c) CV curves of the $FeSe_2$ bars at the beginning, stage II, and stage III under various scan rates in the range of 0.2–1.0 mV s^{-1}. (d–f) Summary of the reduction peak percentages of the $FeSe_2$ bars at different stages. (g–i) CV curves of the large $FeSe_2$ spheres at the beginning, stage II, and stage III under various scan rates in the range of 0.2–1.0 mV s^{-1}. (j–l) Summary of the reduction peak percentages of the large $FeSe_2$ spheres at different stages.

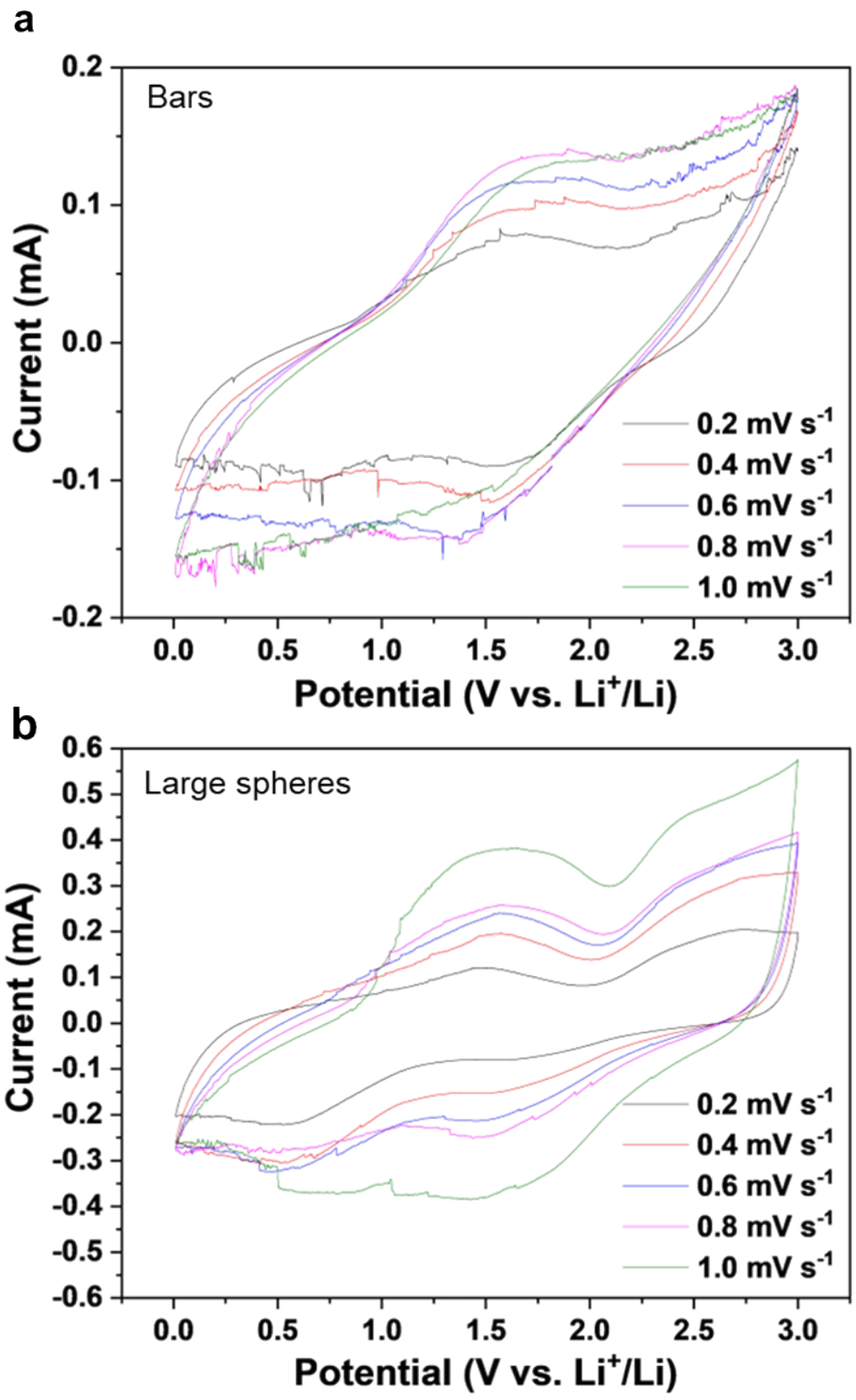

Fig. S12 CV curves of the $FeSe_2$ (a) bars and (b) large spheres at stage IV under various scan rates in the range of 0.2–1.0 mV s^{-1}.

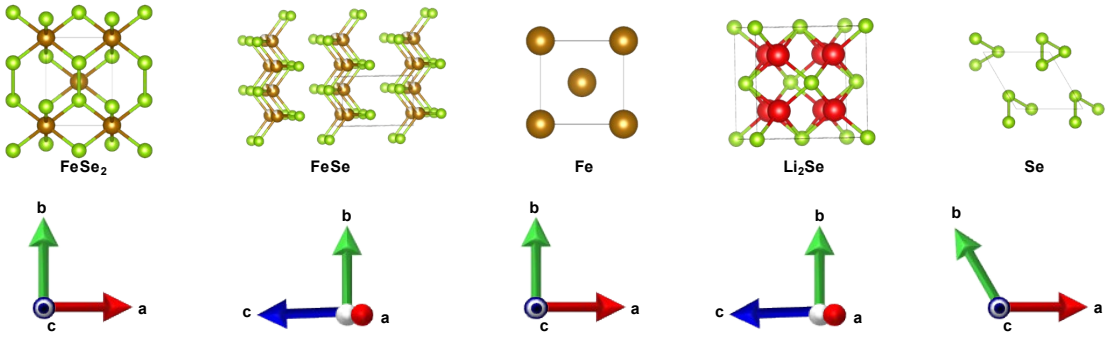

Fig. S13 Orientations of the crystal models.